

Convection in heated fluid layers subjected to time periodic horizontal accelerations

By **W. Pesch¹**, **D. Palaniappan^{1,2}**, **J. Tao^{1,3}**, and **F. H. Busse¹**

¹ Institute of Physics, University of Bayreuth, D-95440 Bayreuth, Germany;

² Department of Mathematics, Texas A&M University, College Station, TX 77843-3368, USA;

³ LTCS and Department of Mechanics and Aerospace Technologies,
Peking University, Beijing 100871, China

(Received 7 October 2007)

A theoretical study is presented of convection in a horizontal fluid layer heated from below or above which is periodically accelerated in its plane. The analysis is based on Galerkin methods as well as on direct numerical simulations of the underlying Boussinesq equations.

Shaking in a fixed direction breaks the original isotropy of the layer. At onset of convection and at small acceleration we find longitudinal rolls, where the roll axis aligns parallel to the acceleration direction. With increasing acceleration amplitude a shear instability takes over and transverse rolls with the axis perpendicular to the shaking direction nucleate at onset. In the nonlinear regime the longitudinal rolls become unstable against transverse modulations very close to onset which leads to a kind of domain chaos between patches of symmetry degenerated oblique rolls.

In the case of circular shaking the system is isotropic in the time average sense, however, with a broken chiral symmetry. The onset of convection corresponds to the transverse roll case studied before with the roll axis selected spontaneously. With increasing Rayleigh number a heteroclinic cycle is observed with the roll changing its orientation periodically in time. At even higher Rayleigh number this heteroclinic cycle becomes chaotic similarly as in the case of the Küppers-Lortz instability.

1. Introduction

The topic of convection in fluid layers heated from below or from above that are subjected to time periodic acceleration has received considerable attention in recent years. The book by Gershuni and Lyubimov (1998) provides a good overview of the numerous cases that are obtained as the direction of acceleration and the inclination of the layer with respect to the horizontal are varied. The case of an extended horizontal layer in the

presence of a periodic *vertical* acceleration has been of special interest since it preserves the property of horizontal isotropy. It has been recently realized in experiments (Rogers et al., 2000, 2003, 2005); the structure of convection exhibits square superlattices besides other types of patterns in excellent agreement with the theoretical predictions.

Another special case is the horizontal fluid layer subjected to *horizontal* accelerations which is the issue of this paper. This problem has first been considered by Gershuni et al. (1996) for a fixed direction of the acceleration and for the single value $P = 1$ of the Prandtl number P in the linear regime. In the present paper we extend these investigations in several ways. We first study the influence of variations of P on the onset of convection and then proceed into the nonlinear regime to capture the stability of finite-amplitude roll solutions. Particular attention will be devoted to the study of a rotation of the acceleration direction in the horizontal plane with constant angular velocity. In this case it must be expected that in the time average horizontally isotropic conditions prevail. In particular chaotic forms of convection are found in this situation, which resemble the domain chaos originating from the Küppers-Lortz instability (Küppers and Lortz (1969); Clever and Busse (1979)) in a convection layer rotating about a vertical axis.

The problem of convection in the presence of time-periodic oscillations is of fundamental interest because of a wide variety of possible new convection patterns and the transition to chaotic flows. The understanding of convective processes in the presence non-stationary force fields has also practical relevance in space technologies such as the growth of crystals (Kozlow et al. (2004)).

In section 2 we shall first discuss the mathematical formulation of our problem and sketch briefly the numerical methods. In section 3 a linear stability analysis of the homogeneous basic state is used to describe the properties of the system at onset of convection. We first deal with cases of uni-directional acceleration, before accelerations that are isotropic in the time averaged sense will be considered. Various destabilization mechanism of convection roll patterns at finite amplitudes are analyzed in section 4. As a consequence a complex spatio-temporal dynamics is excited which is addressed by fully numerical simulations of the basic equations in section 5. The paper closes with a concluding discussion in section 6.

The patterns and their stability depend sensitively on a variety of experimental control parameters, like the dimensionless applied temperature gradient (Rayleigh number), the Prandtl number, the frequency, the direction and the amplitude of the applied acceleration. In selecting interesting regions in the parameter space we have been guided by possibilities for experimental realisations in the laboratory.

2. Mathematical background

We consider a horizontal fluid layer with fixed temperatures $T = T_1$ and $T = T_2$ prescribed at its upper and lower boundaries, respectively, that is subjected to a harmonic acceleration $\mathcal{G}(t)$ with frequency Ω of the form

$$\mathcal{G}(t) = -g(\mathbf{e}_z + \frac{b_x \Omega^2}{g} \mathbf{e}_x \sin \Omega t + \frac{b_y \Omega^2}{g} \mathbf{e}_y \cos \Omega t). \quad (2.1)$$

where $-g\mathbf{e}_z$ is the acceleration of gravity opposite to the direction of the vertical unit vector \mathbf{e}_z . The additional terms are caused by a periodic shaking of the fluid layer with amplitudes b_x, b_y in the horizontal directions described by the unit vectors \mathbf{e}_x and \mathbf{e}_y , respectively. We employ the Boussinesq approximation in that all material properties are regarded as constant, except for the temperature dependence of the density described by $\rho(T) = \rho_0 (1 - \alpha(T - T_0))$, which is kept only in the buoyancy terms. Here $T_0 = (T_1 + T_2)/2$ denotes the average temperature and α is the thermal expansion coefficient. We focus the attention on systems with a large aspect ratio, where the lateral dimensions are much larger than the layer height d .

We use d as length scale and the vertical diffusion time $t_v = d^2/\kappa$ as time scale where κ is the thermal diffusivity of the fluid. Furthermore $\nu\kappa/\alpha g d^3$ is chosen as scale for the deviation Θ of the temperature from its purely conductive state with ν the kinematic viscosity. We thus arrive at the following basic equations in dimensionless form:

$$P^{-1} D_t \mathbf{v} = -\nabla \Pi + (\mathbf{e}_x G_x \sin \omega t + \mathbf{e}_y G_y \cos \omega t)(\Theta - Rz) + \mathbf{e}_z \Theta + \nabla^2 \mathbf{v}, \quad (2.2a)$$

$$D_t \Theta = R \mathbf{e}_z \cdot \mathbf{v} + \nabla^2 \Theta, \quad \text{with } D_t = \frac{\partial}{\partial t} + (\mathbf{v} \cdot \nabla), \quad (2.2b)$$

$$\nabla \cdot \mathbf{v} = 0. \quad (2.2c)$$

Here the Rayleigh number R , the Prandtl number P , the dimensionless frequency ω and acceleration parameters G_x and G_y are defined by

$$R = \frac{\alpha g}{\nu \kappa} (T_2 - T_1) d^3, \quad P = \frac{\nu}{\kappa}, \quad \omega = \frac{\Omega d^2}{\kappa}, \quad G_x = \frac{b_x \Omega^2}{g}, \quad G_y = \frac{b_y \Omega^2}{g}. \quad (2.3)$$

All gradient terms on the right hand side of (2.2a) have been collected into $-\nabla \Pi$. In the limit $G_x = G_y = 0$ the standard Rayleigh-Bénard convection (RBC) problem is recovered.

The velocity field \mathbf{v} can be decomposed as follows:

$$\mathbf{v} = \mathbf{e}_x (R \overline{G_x V_x} + U_x) + \mathbf{e}_y (R \overline{G_y V_y} + U_y) + \mathbf{u}, \quad \text{with } \mathbf{u} = \mathbf{v} - \overline{\mathbf{v}}, \quad (2.4)$$

where the overline indicates the horizontal average. The basic flow $R(\overline{G_x V_x}, \overline{G_y V_y}, 0)$ derives from equation (2.2a) for $\Theta = 0$. Assuming an infinitely extended layer we obtain the following analytical expressions for V_x, V_y which satisfy the no-slip conditions at

$z = \pm 0.5$:

$$V_x(z, t) = \frac{P}{\omega} [z \cos \omega t + Z_1 \cos \omega t + Z_2 \sin \omega t], \quad (2.5a)$$

$$V_y(z, t) = \frac{P}{\omega} [-z \sin \omega t - Z_1 \sin \omega t + Z_2 \cos \omega t], \quad (2.5b)$$

where

$$Z_1 = \frac{\cosh \alpha \cos \beta - \cosh \beta \cos \alpha}{2(\cos \gamma - \cosh \gamma)}, \quad Z_2 = \frac{\sinh \alpha \sin \beta - \sinh \beta \sin \alpha}{2(\cos \gamma - \cosh \gamma)}$$

and

$$\alpha = \gamma \left(\frac{1}{2} + z \right), \quad \beta = \gamma \left(\frac{1}{2} - z \right), \quad \gamma = \sqrt{\frac{\omega}{2P}}.$$

In the limit $\omega \rightarrow 0$, the solution for the basic flow corresponds to a time-periodic cubic shear flow profile

$$V_x(z, t) = \frac{1}{6} \left(z^3 - \frac{z}{4} \right) \sin \omega t, \quad V_y(z, t) = \frac{1}{6} \left(z^3 - \frac{z}{4} \right) \cos \omega t. \quad (2.6)$$

Note the analogy to time-independent inclined layer convection (see e.g. Clever and Busse 1977; Daniels and Bodenschatz 2002). In this case a base flow profile, cubic in z , parallel to the layer is also found.

The equations for the corrections U_x and U_y of the basic flow are obtained by a horizontal average of (2.2a):

$$\partial_{zz}^2 U_x(z, t) = P^{-1} \partial_t U_x + P^{-1} \partial_z (\overline{u_z u_x}) - G_x \overline{\Theta} \sin(\omega t), \quad (2.7a)$$

$$\partial_{zz}^2 U_y(z, t) = P^{-1} \partial_t U_y + P^{-1} \partial_z (\overline{u_z u_y}) - G_y \overline{\Theta} \cos(\omega t). \quad (2.7b)$$

Since the horizontal average of the solenoidal vector field \mathbf{u} (2.4) vanishes the general representation in terms of poloidal and toroidal components,

$$\mathbf{u} = \nabla \times (\nabla f \times \mathbf{e}_z) + \nabla \phi \times \mathbf{e}_z \equiv \boldsymbol{\delta} f + \boldsymbol{\eta} \phi, \quad (2.8)$$

can be used. The equations for the velocity potentials f and ϕ are obtained by operating with $\boldsymbol{\delta}$ and $\boldsymbol{\eta}$ on (2.2a):

$$\begin{aligned} & \nabla^4 \Delta_2 f + G_x \sin \omega t \partial_{xz}^2 \Theta + G_y \cos \omega t \partial_{yz}^2 \Theta - \Delta_2 \Theta \\ &= P^{-1} \left(\boldsymbol{\delta} \cdot [(\boldsymbol{\delta} f + \boldsymbol{\eta} \phi) \cdot \nabla (\boldsymbol{\delta} f + \boldsymbol{\eta} \phi)] \right. \\ &+ [(RG_x V_x + U_x) \partial_x + (RG_y V_y + U_y) \partial_y + \partial_t] \nabla^2 \Delta_2 f \\ &\left. - [(\partial_{zz}^2 (RG_x V_x + U_x)) \partial_x + (\partial_{zz}^2 (RG_y V_y + U_y)) \partial_y] \Delta_2 f \right), \quad (2.9) \end{aligned}$$

$$\begin{aligned} & \nabla^2 \Delta_2 \phi + G_x \sin \omega t \partial_y \Theta - G_y \cos \omega t \partial_x \Theta \\ &= P^{-1} \left(\boldsymbol{\eta} \cdot [(\boldsymbol{\delta} f + \boldsymbol{\eta} \phi) \cdot \nabla (\boldsymbol{\delta} f + \boldsymbol{\eta} \phi)] \right. \\ &+ [(RG_x V_x + U_x) \partial_x + (RG_y V_y + U_y) \partial_y + \partial_t] \Delta_2 \phi \\ &\left. - [(\partial_z (RG_x V_x + U_x)) \partial_y - (\partial_z (RG_y V_y + U_y)) \partial_x] \Delta_2 f \right), \quad (2.10) \end{aligned}$$

where the two-dimensional Laplacian $\Delta_2 = \partial_{xx}^2 + \partial_{yy}^2$ has been introduced. The equation for Θ can now be written in the form

$$\nabla^2 \Theta - R \Delta_2 f = (\delta f + \eta \phi) \cdot \nabla \Theta + \left((RG_x V_x + U_x) \partial_x + (RG_y V_y + U_y) \partial_y + \partial_t \right) \Theta. \quad (2.11)$$

Equations (2.7 -2.11) must be solved subject to the no-slip boundary conditions

$$f = \partial_z f = \phi = \Theta = U_x = U_y = 0 \quad \text{at} \quad z = \pm 0.5. \quad (2.12)$$

As a consequence of our restriction to large aspect ratio cells periodic boundary conditions in the x, y plane are appropriate, which allow a description in terms of 2d-Fourier expansions.

For simplicity, a symbolic notation for the Eqs.(2.7 -2.11) is used in the following,

$$\mathcal{C} \frac{\partial}{\partial t} \mathbf{V}(\mathbf{x}, z, t) = \mathcal{L} \mathbf{V}(\mathbf{x}, z, t) + \mathbf{N}[\mathbf{V}(\mathbf{x}, z, t) | \mathbf{V}(\mathbf{x}, z, t)], \quad \text{with } \mathcal{L} \equiv \mathcal{A} + R \mathcal{B}, \quad (2.13)$$

where the symbolic vector $\mathbf{V} = (\Theta, f, \phi, \mathbf{U})$ represents the different fields in our problem and $\mathbf{x} = (x, y)$. The ground state corresponds to $\mathbf{V}(\mathbf{x}, z, t) \equiv 0$. The operators \mathcal{C} , \mathcal{L} are linear differential operators, \mathbf{N} describes the quadratic nonlinearities. Note that we have made explicit the Rayleigh number R in the definition of \mathcal{L} where the operators \mathcal{A}, \mathcal{B} contain contributions periodic in time with the period $2\pi/\omega$.

In this paper we will mainly study "roll" solutions of the problem posed by Eq. (2.13). They are periodic in the plane (wavelength λ) along a certain direction, which includes an angle χ with the x -axis, as well as periodic in time with frequency ω .

To construct the roll solutions we use a Galerkin representation: $\mathbf{V}(\mathbf{x}, z, t)$ is expanded into suitable complete sets of functions which ensure, that the spatial and temporal periodicities and the boundary conditions (2.12) are satisfied. In this way (2.13) is mapped onto a system of nonlinear coupled ODE's for the corresponding expansion coefficients. For instance the temperature field is represented as:

$$\Theta(\mathbf{x}, z, t) = \sum_{\mathbf{q}} \sum_{n=1}^N \Theta(\mathbf{q}, n, t) \exp[i \mathbf{q} \cdot \mathbf{x}] \sin[n\pi(z + \frac{1}{2})]. \quad (2.14)$$

The \mathbf{q} -vectors in Eq. (2.14) are given as integer multiples of the basis vector $\mathbf{q}_r = q_r(\cos \chi, \sin \chi)$ with $\lambda = (2\pi/q_r)$ of the form $\mathbf{q} = m \mathbf{q}_r$ with $-M \leq m \leq M$.

For the velocity potentials $f(\mathbf{x}, z, t), \phi(\mathbf{x}, z, t)$ we use analogous representations, except that for f the Chandrasekhar (1961) functions $C_n(z)$ replace the trigonometric functions in (2.14). The reality of all fields requires $\Theta(\mathbf{q}, n, t) = \Theta^*(-\mathbf{q}, n, t)$, etc., where the star indicates the complex conjugate.

By representing $\Theta(\mathbf{q}, n, t)$ as the Fourier series:

$$\Theta(\mathbf{q}, n, t) = \sum_{k=-K}^K \theta(\mathbf{q}, n|k) \exp[i k \omega t] \quad (2.15)$$

the periodicity of Θ in time, i.e. $\Theta(\mathbf{x}, z, t) = \Theta(\mathbf{x}, z, t + 2\pi/\omega)$, is guaranteed as well. An analogous expansion for $f(\mathbf{q}, n, t), \phi(\mathbf{q}, n, t)$ defines their expansion coefficients $f(\mathbf{q}, n|k)$ and $\phi(\mathbf{q}, n|k)$, respectively. The correction $\mathbf{U}(z, t) = (U_x, U_y, 0)$ of the basic flow is represented as follows:

$$\mathbf{U}(z, t) = \sum_{n=1}^N \sum_{k=-K}^K \mathbf{U}(n|k) \sin[n\pi(z + \frac{1}{2})] \exp[i k \omega t]. \quad (2.16)$$

The sums appearing for instance in (2.14, 2.15, 2.16) have to be truncated. For the range of parameters considered in this paper we have mostly used the truncation parameters $N = 5, K = 7, M = 3$, which requires already the solution of 2040 nonlinear equations for the expansion coefficients in the nonlinear regime. To test the accuracy of our results we have increased N, K, M separately in steps of two, until the changes remained less than 1%.

Let us first focus on the case of *unidirectional* shaking, $G_y = 0$. We have to distinguish two relevant cases namely the longitudinal rolls ($\chi = \pi/2, \mathbf{q}_r = (0, p)$), which depend only on y and the transverse rolls ($\chi = 0, \mathbf{q}_r = (q, 0)$) which depend only on x .

For transverse rolls one deduces $U_y = \phi \equiv 0$ from (2.7, 2.10). Furthermore inspection of (2.7-2.11) shows that the transformation:

$$\mathcal{T}_x : (x, z, t) \rightarrow (x + \frac{\pi}{q}, -z, t + \frac{\pi}{\omega}) \quad (2.17)$$

either reproduces or reverses the sign of the spatially and temporally periodic solutions,

$$\mathcal{T}_x(U_x, \Theta, f) \rightarrow \mathbf{p}(U_x, -\Theta, -f) \quad \text{with } \mathbf{p} = \pm 1. \quad (2.18)$$

Near onset the roll solutions show almost exclusively the even-parity ($\mathbf{p} = 1$) signature.

The case of *longitudinal* rolls ($\chi = \pi/2$) is simpler. The fields Θ and f are not influenced by shaking (i.e. they are time independent) and reduce thus to the standard RBC solutions without shaking. In contrast to the transverse case ϕ and U_y are finite. In close analogy to \mathcal{T}_x a transformation \mathcal{T}_y can be defined as

$$\mathcal{T}_y : (y, z, t) \rightarrow (y + \frac{\pi}{p}, -z, t + \frac{\pi}{\omega}), \quad (2.19)$$

which again either reproduces the periodic solutions or reverses their sign:

$$\mathcal{T}_y(U_x, U_y, \Theta, f, \phi) \rightarrow \mathbf{p}(U_x, U_y, -\Theta, -f, \phi) \quad \text{with } \mathbf{p} = \pm 1. \quad (2.20)$$

Near onset only the even parity case $\mathbf{p} = 1$ is realized in our case.

We now turn to *uniformly rotating* acceleration with $G_x = G_y$ which can be realized by superimposing periodic shaking in two orthogonal directions with a phase shift of $\pi/2$ in time (see (2.1)). Thus the longitudinal steady roll solution does not exist. On the other hand, it is easy to see that the roll solution characterized by a wavevector $\mathbf{q} = (q, 0)$ coincides with the transverse solution in the unidirectional case with respect to the Θ and f components. In addition, however, we have a nonzero toroidal potential ϕ , which

is slaved to Θ, f . Obviously the roll solutions are highly degenerate: for any solution characterized by a basis wavevector $\mathbf{q}_r = (q, 0)$ (see (2.14)) there exists a continuous manifold of equivalent solutions of the same form with a rotated wave vector $\mathbf{q}_r = q_r(\cos \chi, \sin \chi)$, where the arguments $[i k \omega t]$ of the exponential functions inside the time expansion of the form (2.15) are replaced by $[i k(\omega t + \chi)]$.

3. Linear analysis

In order to investigate the stability of the basic state we linearize (2.13) about $\mathbf{V} \equiv 0$, i.e. we neglect the nonlinearity \mathbf{N} . There is no need to consider (2.10) since ϕ does not enter the linearized versions of (2.9, 2.11). Once f and Θ have been determined the toroidal contribution to the velocity \mathbf{u} can be computed.

As a consequence of the explicit periodic time dependence of the linear operator the linearized equations are solved with the Floquet ansatz:

$$\mathbf{V}(\mathbf{x}, z, t) = \exp[\sigma t + i\mathbf{q} \cdot \mathbf{x}] \mathbf{V}_{lin}(\mathbf{q}, z, t); \quad \mathbf{q} = (q, p), \quad \mathbf{x} = (x, y) \quad (3.1)$$

with $\mathbf{V}_{lin}(\mathbf{q}, z, t) = \mathbf{V}_{lin}(\mathbf{q}, z, t + 2\pi/\omega)$. Thus we arrive at the linear eigenvalue problem:

$$\sigma(\mathbf{q}, R) \mathcal{C} \mathbf{V}_{lin}(\mathbf{q}, z, t) = (\mathcal{A} + R\mathcal{B} - \mathcal{C} \frac{\partial}{\partial t}) \mathbf{V}_{lin}(\mathbf{q}, z, t). \quad (3.2)$$

We are interested in the growth rate, $\sigma_0(\mathbf{q}, R)$, i.e. the eigenvalue $\sigma(\mathbf{q}, R)$ with the largest real part. The condition $Re[\sigma_0(\mathbf{q}, R)] = 0$ yields the neutral surface $R_0(\mathbf{q})$ with its minimum values R_c (the critical Rayleigh number) at the critical wave vector \mathbf{q}_c .

Eq. (3.2) is solved by the Galerkin method as discussed in the preceding section, which includes, for instance, the following ansatz for the temperature component, Θ_{lin} , of $\mathbf{V}_{lin}(\mathbf{q}, z, t)$:

$$\Theta_{lin}(\mathbf{q}, z, t) = \sum_{n=1}^N \sum_{k=-K}^K \theta_{lin}(\mathbf{q}, n|k) \exp[i k \omega t] \sin n\pi(z + 1/2). \quad (3.3)$$

The analogous expansion for the f component of \mathbf{V}_{lin} is characterized by the expansion coefficients $f_{lin}(\mathbf{q}, n|k)$. Thus we arrive at a linear algebraic eigenvalue problem, which yields $\sigma_0(\mathbf{q}, R)$ and the corresponding expansion coefficients θ_{lin}, f_{lin} of the linear eigenvector.

If the imaginary part of $\sigma_0(\mathbf{q}, R)$ vanishes together with its real part at $\mathbf{q} = \mathbf{q}_c, R = R_c$ the bifurcation is stationary; otherwise we speak of an oscillatory (Hopf) bifurcation. In fact we did not find oscillatory bifurcations in the present system and $Im[\sigma_0(\mathbf{q}, R_0(\mathbf{q}))] = 0$ does hold near the minimum of the neutral curve ($\mathbf{q} \approx \mathbf{q}_c$) in all cases. Note that in this case the neutral curve $R = R_0(\mathbf{q})$ can directly be identified with the smallest eigenvalue $\tilde{\lambda}$ of the (generalized) eigenvalue problem $(\mathcal{A} - \mathcal{C} \partial/\partial t + \tilde{\lambda} \mathcal{B}) \mathbf{V}_{lin} = 0$ (see Eq. 3.2) and can thus be calculated numerically without much effort.

At first inspection our general finding $Im[\sigma_0(\mathbf{q}_c, R_c)] = 0$ looks surprising. Typically for

the majority of periodically driven systems there exists the possibility of a subharmonic bifurcation, i.e. $Im[\sigma_0(\mathbf{q}_c, R_c)] = \omega/2$. However, the driven oscillations investigated in this paper belong to a category that does not exhibit subharmonic responses in contrast to the case of a vertically oscillated convection layer (Rogers et al. (2005)).

The origin for the absence of a subharmonic instability has been well elucidated in a paper by Or(1996), see also Schulze (1999). When the representation (3.3) for Θ and the corresponding ones for f and ϕ are inserted into the linearized equations (2.7 -2.11), one arrives at the following linear system for the "vector" \mathbf{v} of the expansion coefficients:

$$\frac{d\mathbf{v}}{d\theta} = [\mathbf{A} + i\mathbf{P}(\theta)]\mathbf{v} \quad (3.4)$$

which is identical to Eq. (A.1) in Or (1997) or Eq. (2) in Schulze (1999) with $\theta = \omega t$. The matrices \mathbf{A}, \mathbf{P} are real and the condition $\mathbf{P}(\theta + \pi) = -\mathbf{P}(\theta)$ holds. Thus Eq.(3.4) possesses the conjugate-translation symmetry according to which $\mathbf{v}^*(\theta + \pi) = K\mathbf{v}(\theta)$, where K is an arbitrary complex constant. As a consequence subharmonic solutions are precluded (Or (1997); Schulze (1999)).

As a result of the symmetries of our problem discussed before in connection with equations (2.18, 2.20) the possible eigenvectors separate into two classes. The first one (even parity, $\mathbf{p} = 1$) is characterized by $\theta(\mathbf{q}_c, n|k) = f(\mathbf{q}_c, n|k) = 0$ for even $|k+n|$, while for the second, odd-parity class $\theta(\mathbf{q}_c, n|k) = f(\mathbf{q}_c, n|k) = 0$ holds for odd $|k+n|$. As in the standard RBC case the even parity-class yields almost exclusively the critical properties, where we found the coefficient $\theta(\mathbf{q}_c, n = 1|k = 0)$ to be the leading one.

In the following we will separately investigate the case of unidirectional shaking ($G_y = 0$) and of circular shaking ($G_x = G_y$).

3.1. Linear analysis for unidirectional shaking

In this section we focus on the special case $G_y = 0$. There are two distinguished types of solutions of the form (3.1):

- *Longitudinal* roll solutions with wavevector $\mathbf{q} = (0, p)$ which are time independent and where the neutral curve $R_{y0}(p) \equiv R_0(\mathbf{q})$ and thus its minimum $R_{y0}(p_c) \equiv R_y = 1708$ at the critical wavevector $\mathbf{q}_c = (0, p_c)$ with $p_c = 3.117$ does not depend on the system parameters. This solution is thus identical to the two-dimensional RBC solution in the absence of shaking except for an additional oscillating component $u_x(y, z, t)$ of \mathbf{u} arising from the toroidal potential $\phi(y, z, t)$ (see (2.8, 2.10)) an example of which is shown in figure 1. Its sinusoidal dependence on time reflects the buoyancy of the horizontal acceleration and the advection of the vertical velocity component of the longitudinal rolls by the oscillatory base flow. The other velocity components are only affected when the longitudinal rolls become unstable to three-dimensional disturbances in the nonlinear regime as will be discussed in section 4.

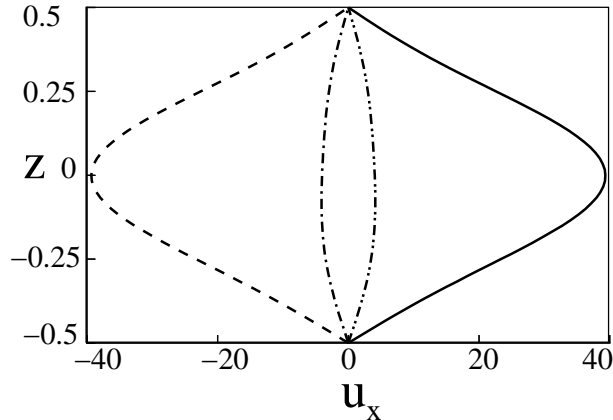


FIGURE 1. Velocity component u_x (arbitrary units) parallel to the axis of longitudinal convection rolls for $G_x = 3.6$, $\omega = 50$ and $P = 1$. The solid, dash-dotted, dashed and dash-double dotted lines show the z -profiles at $y = 0$ for the different times $t = n\pi/(2\omega)$ with $n = 0, 1, 2, 3$, respectively.

- *Transverse* roll solutions with $\mathbf{q} = (q, 0)$ for which the neutral curve $R_{x0}(q) \equiv R_0(\mathbf{q})$ and its minimum $R_{x0}(q_c) \equiv R_x$ together with the critical wavevector $\mathbf{q}_c = (q_c, 0)$ become complicated functions of the parameters G_x, P and ω .

The analysis of general 3d-solutions with $\mathbf{q} = (q, p)$ reveals that for arbitrary values of the parameters G_x, P, ω either the longitudinal or the transverse roll solutions yield the critical Rayleigh number. Since the longitudinal rolls are well understood from standard RBC we shall restrict the discussion to the solutions of the transverse roll type.

In figures 2, 3, 4 the critical Rayleigh numbers R_x for the onset of transverse rolls have been plotted as functions of G_x and ω for three different Prandtl numbers. The curves for R_x always start $G_x = 0$ with the RBC value of $R_x = 1708$ and increase, owing to the stabilizing influence of the shear, with increasing G_x as long as ω is sufficiently small. At the same time the wavenumber q decreases in order to diminish the effect of the shear on the convection rolls. For sufficiently high values of G_x , however, the time dependent shear becomes destabilizing at Prandtl numbers of the order unity or less and leads to decreasing values of R_x with increasing G_x . The transition from the stabilizing to the destabilizing role of the shear is shifted to increasing values of G_x with increasing ω . For values of ω in excess of 33 (50) in the cases of $P = 0.5$ ($P = 1$), this scenario is modified in that $R_x < R_y = 1708$ already at small values of G_x as can be seen in figures 2 and 3.

The structure of the transverse roll solutions as a function of time is displayed in figures 5 and 6 for two exemplary cases. The graphs are based on the Galerkin solutions near onset at $\epsilon = (R - R_x)/R_x = 0.2$. While the spatial dependence in the weakly nonlinear regime reflects the linear solutions at onset, we obtain in this way some finite amplitude properties as well as, for instance, the modifications of the basic flow \mathbf{U} . Although in figure 5 the oscillatory shear exerts a stabilizing influence while the opposite effect occurs

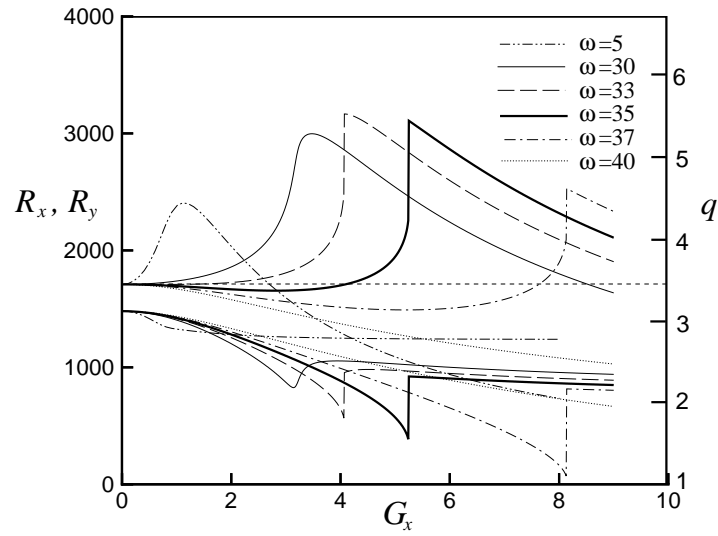


FIGURE 2. Critical Rayleigh numbers R_x for the onset of transverse roll convection at $P = 0.5$ as functions of G_x for different values of ω as indicated. Corresponding values of the critical wavenumbers q (measured on the right ordinate) are given by the lower set of lines. Also indicated by the thin short-dashed line is the value $R_y = 1708$ for the onset of longitudinal rolls.

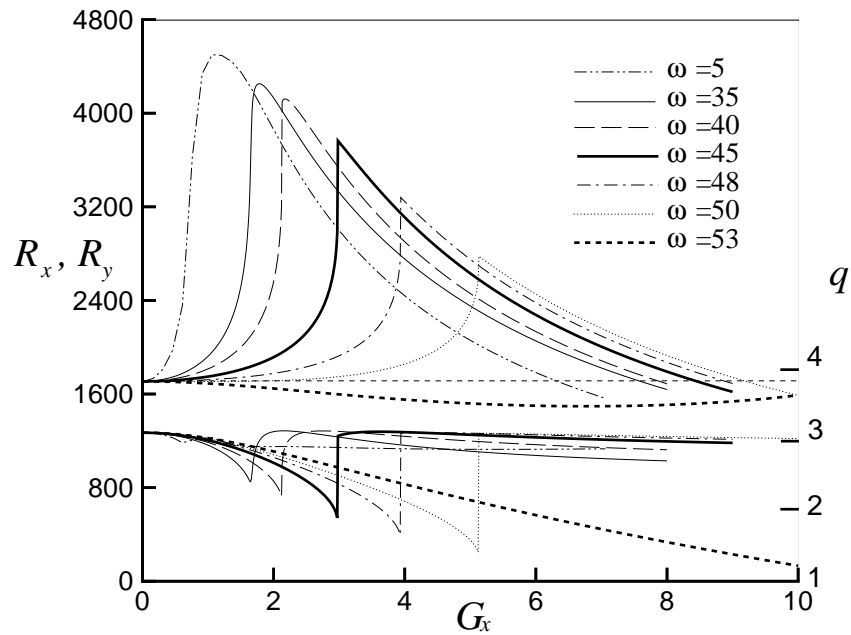


FIGURE 3. Same as figure 2, but in the case $P = 1$.

in the case of figure 6, the velocity structures are rather similar in both cases. Only the

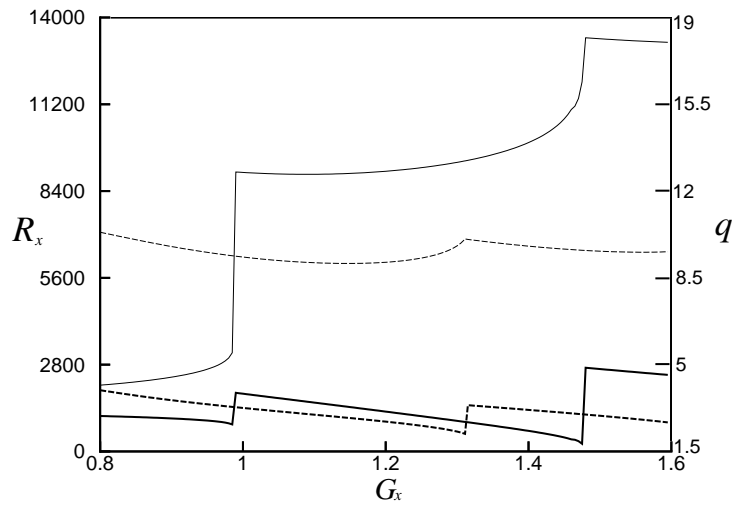


FIGURE 4. Critical Rayleigh numbers R_x (thin lines) for the onset of transverse roll convection at $P = 6$ as functions of G_x for $\omega = 50$. Corresponding values of the critical wavenumbers q_c (measured on the right ordinate) are given by the lower set of thick lines. Solid (dashed) lines correspond to the even (odd) parity case.

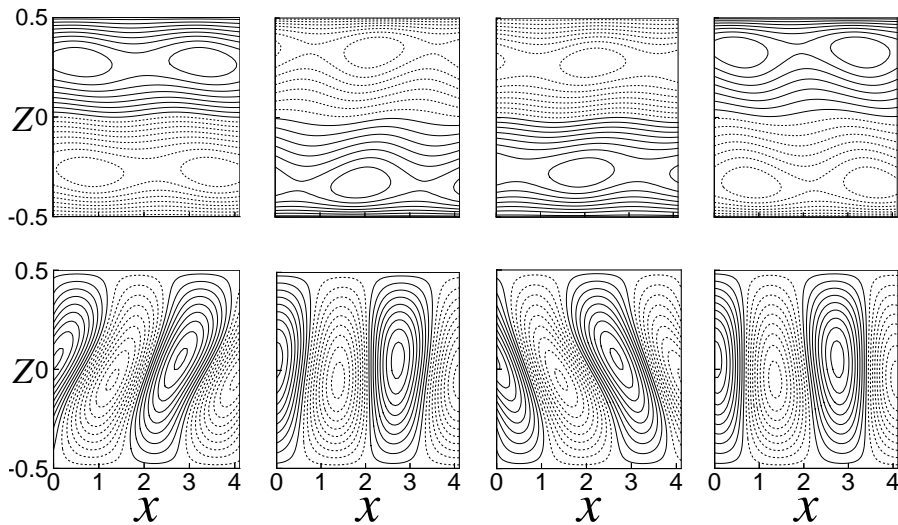


FIGURE 5. Lines of constant velocity v_x in transverse roll convection at four different times (upper row, $t = n\pi/2\omega$, $n = 0, 1, 2, 3$, from left to right) in the case $G_x = 3.6$, $\omega = 50$ and $P = 1$. Corresponding isotherms of Θ are displayed in the lower row. Solid (dashed) lines indicate positive (negative) values.

fluctuating component of the temperature exhibits the inhibiting influence of the stronger shearing action in the case of figure 6.

The rather rapid changes, kinks and even jumps in the dependence of the critical Rayleigh number R_x on G_x for larger values of the latter parameter correspond to the

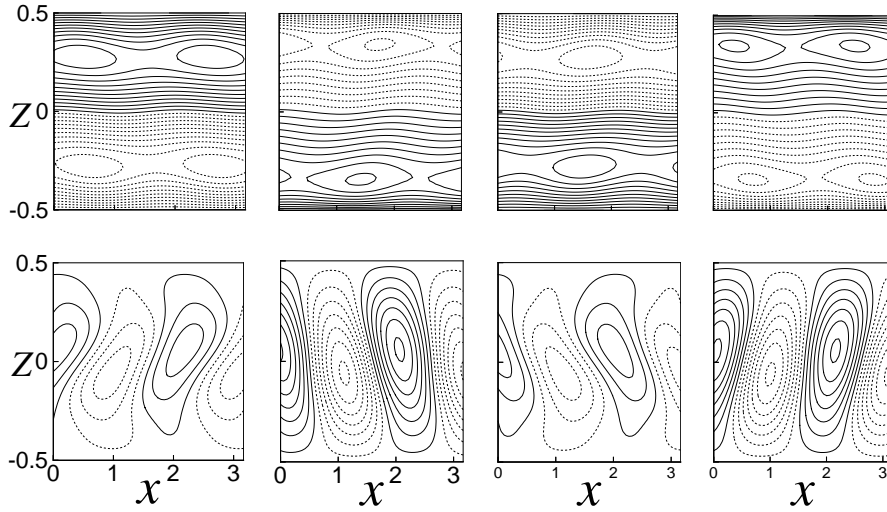


FIGURE 6. Same as figure 5, but in the case $G_x = 12.5$, $\omega = 50$ and $P = 1$.

appearance of double minima of the neutral curve $R_{x0}(q)$ and are reflected in the jumps of the critical wavenumber q_c which also have been plotted in the figures. Jumps in the values of R_x are obtained when the neutral curves $R_{x0}(q)$ form isolas as shown for example in figure 7. The eigenfunctions $\mathbf{V}_{lin}(x, z, t)$ corresponding to the curves in figures 2 and 3 have always even parity. In the case of $P = 6$ as shown in figure 4, however, the even-parity mode is replaced by the odd-parity mode as the preferred one when G_x exceeds a value of the order unity. As the Prandtl number decreases the critical Rayleigh number for the onset of the antisymmetric mode increases and for $P < 2$ the symmetric mode is preferred. The curves of figure 4 have been plotted for only a single value of ω since for other values the curves are rather similar except for a shift in G_x . In the case $\omega = 40$, for example, the antisymmetric mode replaces the symmetric one already at $G_x = 0.85$.

Of some interest is also the onset of instability in the case of negative Rayleigh numbers, i.e. in the presence of a stably stratified density distribution caused by heating from above. The basic state is still described by the flow $\mathbf{e}_x R G_x V_x$ (2.7) and the corresponding linear temperature profile, but $T_2 - T_1$ and thus R are now negative. The results of the stability analysis are shown in figures 8 and 9. Since the instability is caused by the shear of the basic flow the relation $-R_x G_x = const.$ may be expected for the critical Rayleigh number $-R_x$. Because of the additional stabilizing buoyancy effects, however, $|R_x|$ decreases with increasing G_x more strongly than G_x^{-1} .

The results for the onset of transverse roll instabilities for positive as well as negative values of R_x can be compared with the corresponding results obtained in the case $P = 1$ by Gershuni et al. (1996). Good agreement has been found. It should be noted that

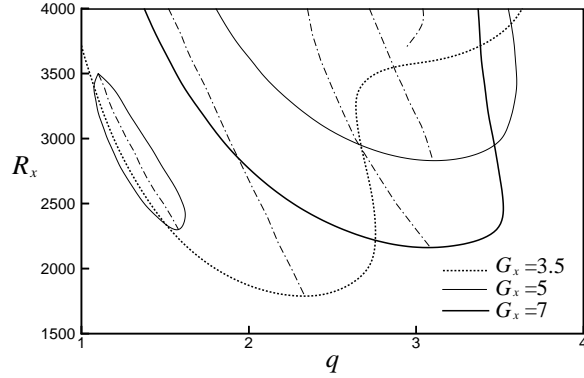


FIGURE 7. Neutral curves R_{0x} as functions of q for three values of G_x as indicated in the case $P = 1, \omega = 50$.

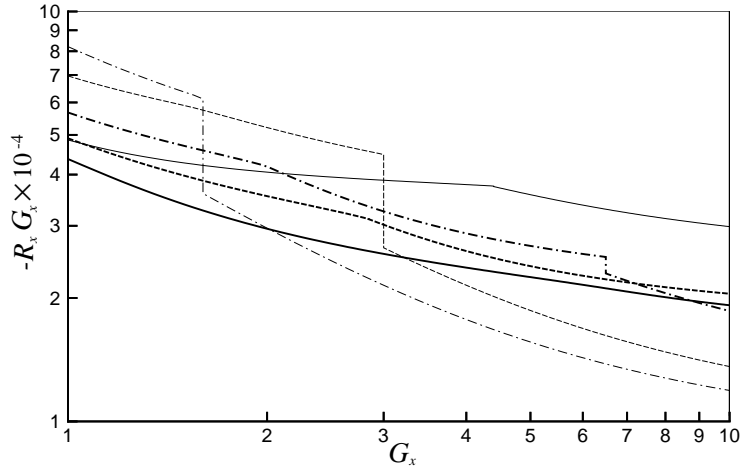


FIGURE 8. The negative critical Rayleigh numbers $-R_x$ (multiplied by G_x) for the onset of transverse roll instabilities in the cases $P = 0.5$ (thin lines) and $P = 1$ (thick lines) as functions of G_x for $\omega = 40$ (solid lines), $\omega = 50$ (dashed lines), $\omega = 60$ (dash-dotted lines).

Gershuni et al. use R and RG_x as independent parameters, while we have chosen R and G_x .

3.2. Linear analysis for circular shaking

In this section we consider the critical properties in the case of circular shaking with $G_x = G_y$. As already discussed at the end of Sect. 2 the transverse roll solutions for the unidirectional acceleration describe the present situation as far as Θ and f are concerned. As a consequence the linear results shown in Figures 2 through 10 can be directly used in the circular case $G_x = G_y$. Figures 5 and 6, however, have to be supplemented by the velocity component v_y perpendicular to x, z -plane, which is shown in figure 10 for the same parameters.

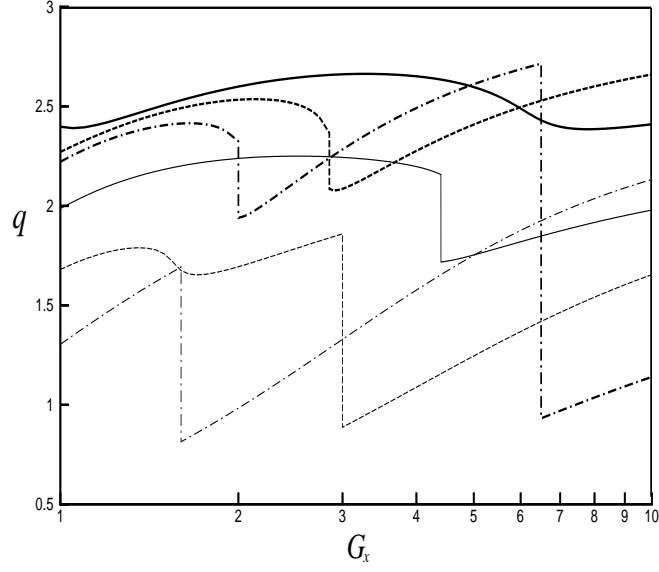


FIGURE 9. Values of the critical wave numbers q_c corresponding to the parameter values shown in figure 8

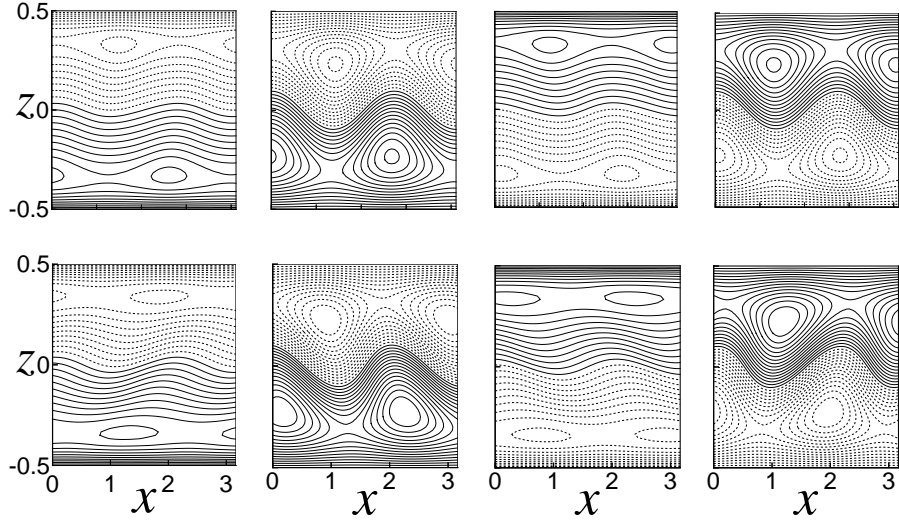


FIGURE 10. Lines of constant velocity component v_y in the x, z -plane of transverse convection rolls at $G_x = G_y$ for the same times and parameters as displayed in figures 5 (upper row) and 6 (lower row).

4. Instabilities of convection rolls at finite amplitudes

To investigate the nonlinear regime we generate first the finite amplitude roll solutions near onset for $q = q_c$ and $R \gtrsim R_0(q_c) = R_c$ in the framework of the familiar weakly

nonlinear analysis, where one starts with the following ansatz:

$$\mathbf{V}_{roll}(\mathbf{x}, z, t) = A(\mathbf{q}_c, t) \mathbf{V}_{lin}(\mathbf{q}_c, z, t) \exp(i\mathbf{q}_c \cdot \mathbf{x}) + c.c. + h.o.t.. \quad (4.1)$$

Here h.o.t denotes higher-order terms and \mathbf{V}_{lin} is the eigenvector for $\sigma_0(\mathbf{q}_c, R)$ (see (3.2)). For the following it is convenient to extract the factor $\tau_0(\mathbf{q})$ (the correlation time) from the linear growthrate $\sigma_0(\mathbf{q}, R)$ (see Sec. 3) and to use instead:

$$\begin{aligned} \tilde{\sigma}(\mathbf{q}, R) &\equiv \tau_0(\mathbf{q}) \sigma_0(\mathbf{q}, R) \approx \epsilon - \frac{R_0(\mathbf{q}) - R_c}{R_c}, \\ \text{with } R &= (1 + \epsilon)R_c, \quad \tau_0^{-1}(\mathbf{q}) = \left. \frac{\partial \sigma_0(\mathbf{q}, R)}{\partial \epsilon} \right|_{\epsilon=0}. \end{aligned} \quad (4.2)$$

Inserting (4.1) into the Boussinesq equations (2.7 -2.11) and systematically expanding in terms of the small amplitude $A(\mathbf{q}_c, t)$ up to cubic order one arrives at the amplitude equation (Cross and Hohenberg (1993)):

$$\tau_0(\mathbf{q}_c) \frac{d}{dt} A(\mathbf{q}_c, R, t) = \tilde{\sigma}(\mathbf{q}_c, R) A - c|A|^2 A \quad (4.3)$$

where $\tilde{\sigma}(\mathbf{q}_c, R) = \epsilon = (R - R_c)/R_c$ (see (4.2)). In all cases a positive cubic coefficient c has been found. The bifurcation from the basic state is thus supercritical and the amplitude is obtained as $|A_0|^2 = \tilde{\sigma}(\mathbf{q}_c, R)/c = \epsilon/c$.

The knowledge of A_0 yields immediately the solution \mathbf{V}_{roll} near onset. The latter is then used as a convenient starting point to construct the fully nonlinear roll solutions $\mathbf{V}_{roll}(\mathbf{x}, z, t)$ in terms of a Galerkin expansion like (2.14, 2.15). A Newton-Raphson method is used to determine the expansion coefficients.

The stability of rolls is examined as usual by a linearization of (2.13) about the steady solution $\mathbf{V}_{roll}(\mathbf{x}, z)$ with its spatial symmetry in the horizontal plane characterized by the wavevector \mathbf{q} ,

$$\mathbf{V}(\mathbf{x}, z, t) = \mathbf{V}_{roll}(\mathbf{x}, z, t) + \exp[\sigma_n t + i\mathbf{s} \cdot \mathbf{x}] \delta\mathbf{V}(\mathbf{x}, z, t). \quad (4.4)$$

Here $\mathbf{s} = (s_x, s_y)$ denotes the Floquet wavevector and σ_n the disturbance growth rate. Furthermore $\delta\mathbf{V}$ satisfies $\delta\mathbf{V}(\mathbf{x}, z, t) = \delta\mathbf{V}(\mathbf{x}, z, t + 2\pi/\omega)$ and shares the spatial symmetry with \mathbf{V} .

In our numerical framework the perturbation $\delta\mathbf{V}(\mathbf{x}, z, t)$ is represented as a Galerkin ansatz of the type shown in (2.14). From (2.13) we thus arrive at a linear eigenvalue problem for the corresponding expansion coefficients, which determines $\sigma_n(\mathbf{q}, R, \mathbf{s})$. The lowest value of R for which the condition $Re[\sigma_n(\mathbf{q}, R, \mathbf{s})] = 0$ holds determines the secondary bifurcations from the roll state.

The nature of the destabilizing modes is characterized by the modulus $|\mathbf{s}|$ and the angle $\psi = \angle(\mathbf{s}, \mathbf{q})$ between \mathbf{s} and the wave vector \mathbf{q} of the roll pattern. A comprehensive exploration of the stability regimes of rolls is outside the scope of this paper in view of

the numerous additional parameters G_x, G_y, ω, P in our problem. We have thus focussed the attention on the stability analysis of rolls close to the onset without being exhaustive.

From our fully nonlinear stability analysis it has turned out, that the modulational modes characterized by $|\mathbf{s}| \rightarrow 0$ are of particular importance. Due to the translational invariance in the x, y plane any mode of the form $\delta\mathbf{V} = (\hat{\mathbf{e}} \cdot \nabla) \mathbf{V}(\mathbf{x}, z, t)$, where $\hat{\mathbf{e}}$ is an arbitrary unit vector in the horizontal plane, is marginally stable, i.e. $\sigma_n(\mathbf{q}, R, \mathbf{s} \rightarrow 0) = 0$. Since the cases \mathbf{s} and $-\mathbf{s}$ (or ψ and $\psi - 180^\circ$) are equivalent due to inversion symmetry, we have $Re[\sigma_n(\mathbf{q}, R, \mathbf{s})] = \tilde{c}(q, \psi)s^2$ for $s \rightarrow 0$ and thus $\tilde{c}(R, q, \psi) = 0$ determines the long-wavelength stability limits of rolls in the R, \mathbf{q} plane.

It is well known that modulational instabilities can be captured near onset in the framework of the weakly nonlinear analysis. Using the ansatz

$$\delta\mathbf{V}(\mathbf{x}, z, t) = \exp[\sigma_n t] \left(B_1(\mathbf{q}_c + \mathbf{s}, t) \mathbf{V}_{lin}(\mathbf{q}_c + \mathbf{s}, z, t) \exp[i(\mathbf{q}_c + \mathbf{s}) \cdot \mathbf{x}] + B_2(-\mathbf{q}_c + \mathbf{s}, t) \mathbf{V}_{lin}(-\mathbf{q}_c + \mathbf{s}, z, t) \exp[-i(\mathbf{q}_c - \mathbf{s}) \cdot \mathbf{x}] \right) \quad (4.5)$$

one arrives at the following algebraic linear eigenvalue problem

$$\begin{aligned} \tau_0(\mathbf{q}_c)\sigma_n B_1 &= \tilde{\sigma}_1 B_1 - a_{11} |A_0|^2 B_1 - \rho_{12} |A_0|^2 B_2, \\ \tau_0(\mathbf{q}_c)\sigma_n B_2 &= \tilde{\sigma}_2 B_2 - a_{22} |A_0|^2 B_2 - \rho_{21} |A_0|^2 B_1 \end{aligned} \quad (4.6)$$

with $\tilde{\sigma}_1 = \tilde{\sigma}(\mathbf{q}_c + \mathbf{s}, R)$ and $\tilde{\sigma}_2 = \tilde{\sigma}(-\mathbf{q}_c + \mathbf{s}, R)$. With the help of our numerical codes we are able to calculate all the coefficients in Eqs. (4.6) for an arbitrary set of our system parameters and thus the maximal growthrate σ_n can be determined.

First we discuss the *unidirectional shaking* case. The stability of *longitudinal* rolls with $\mathbf{q}_c = (0, p_c)$, $R_c = 1708$ is dominated near onset, according to the fully nonlinear Galerkin stability analysis, by the wavy instability with $\psi = 90^\circ$ and $\mathbf{s} = (s, 0)$. The weakly nonlinear approach (4.6) is well suited for understanding the instability mechanism. The coefficients $a_{i,i}, \rho_{i,j}$ are real in this case and for symmetry reasons we have $\tilde{\sigma}_1 = \tilde{\sigma}_2, a_{11} = a_{22}$ and $\rho_{12} = \rho_{21}$. We thus obtain for the maximal disturbance growth rate:

$$\tau_0 \sigma_n = \tilde{\sigma}_1 + (\rho_{12} - a_{11}) |A_0|^2. \quad (4.7)$$

In the limit $s \rightarrow 0$ the following relations hold:

$$\begin{aligned} \tilde{\sigma}_1 &= \epsilon - G_x^2 b_1 s^2 + O(s^4) + O(G_x^4), \\ \rho_{12} - a_{11} &= -c + (-f_0 + f_1 G_x^2) s^2 + O(s^4) + O(G_x^4). \end{aligned} \quad (4.8)$$

The coefficient $f_0 > 0$ depends only on the Prandtl number, while b_1 and $f_1 > 0$ depend in addition on ω . The coefficient b_1 is positive for small ω , where $R_y < R_x$ or equivalently $\tilde{\sigma}_1 < 0$ for $\epsilon = 0$. When ω increases b_1 decreases until it changes sign (e.g. for $P = 1$ at $\omega = 50$ in Fig. 11) when $R_x = R_y$. At larger ω where $\sigma_n \gtrsim 0$ at $\epsilon = 0$ and $R_y < R_x$ the longitudinal rolls are unstable immediately at onset at small G_x .

For $b_1 > 0$ the onset of the wavy instability requires a finite ϵ , $\epsilon > \epsilon_{wav}$, where ϵ_{wav} is obtained from $\sigma_n = 0$ as

$$\epsilon_{wav} = \frac{c G_x^2 b_1}{-f_0 + f_1 G_x^2} + O(G_x^4), \quad (4.9)$$

whenever this expression possesses a positive right hand side, i.e. when $G_x^2 > f_0/f_1$. The stability boundaries $\epsilon = \epsilon_{wav}$ in the ω, G_x plane are shown in figure 11. They are nearly indistinguishable from the full Galerkin results.

Let us consider the case $P = 1$ in more detail. It is sufficient to consider only the regime $\omega < 50$ (i.e. $b_1 < 0$) to the left of the dashed-dotted vertical line in figure 11; for $\omega > 50$ the longitudinal rolls are already unstable at $\epsilon = 0$ with respect to the transverse ones according to figure 3. For sufficiently large G_x the curves for different $\epsilon = \epsilon_{wav}$ approach the limit $\epsilon_{wav} = b_1/f_1$ according to (4.9). Like b_1 also f_1 decreases with increasing ω , while f_0 stays constant. Approaching $\omega = 50$, where $b_1 = 0$, from below all stability boundaries meet at $G_x = f_0/f_1$. For $P = 2$ the coefficient f_1 is smaller and the stability boundaries for small ω and $G_x < 2.5$ will be found only at much larger values of ϵ which have not been calculated. The coefficient b_1 vanishes in this case at $\omega \approx 70$, where all ϵ_{wav} curves meet in analogy to the situation at $P = 1$.

As a general result, longitudinal rolls at moderate values of P become unstable almost at onset, i.e. at very small ϵ . In principle this result is not surprising because of the strong shearing action in our system. Similar results have been found in inclined layer convection (Clever and Busse (1977); Daniels and Bodenschatz (2002)).

A detailed discussion of the wavy instability on the basis of amplitude equations has been presented in Auer and Busse (1994, 1997). There the wavy instability of longitudinal rolls induced by a steady shear flow (which applies to the low- ω case in our system) has been studied for arbitrary values of P and arbitrary wave numbers $p \approx p_c$. In particular the connection to the familiar zig-zag instability line, $\epsilon_{zz} = b_3(p_c - p)$, $b_3 > 0$, in the isotropic limit $G_x \rightarrow 0$ has been established.

It is obvious that *transverse* rolls are unstable against the longitudinal ones in the case of unidirectional shaking for not too large G_x since their critical Rayleigh number R_x is larger than $R_y = 1708$. Conversely, for larger G_x we found the transverse rolls, which bifurcate at threshold for moderate P (see Figs. 2, 3) to be stable near onset.

Let us now turn to the case of *circular shaking* where *transverse* rolls with $\mathbf{q} = \mathbf{q}_c = (q_c, 0)$ bifurcate at onset. The analysis of their stability has revealed a characteristic shortwave instability, which is produced by a mode with wavevector \mathbf{q}_1 ($|\mathbf{q}_1| = q_c$) that includes with \mathbf{q} an angle $\tilde{\psi}$ between 20° and 30° . The instability sets in right at onset for a wide range of ω and $G_x = G_y$. The solid line in Fig. 12 indicates the boundary of this range. The angle $\tilde{\psi}$ of the fastest growing mode along the transition curve has

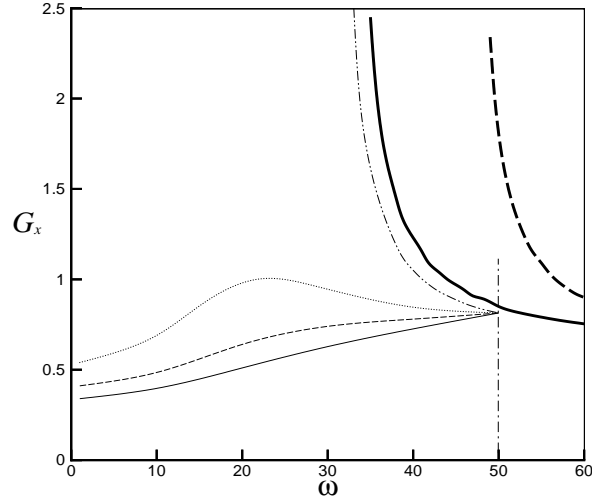


FIGURE 11. Onset of the wavy instability of longitudinal convection rolls as a function of G_x and of ω for $P = 1$ (thin lines) and $P = 2$ (thick lines). Positive growth rates are found for $P = 1$ above the curves corresponding to $\epsilon_{wav} = 0.03$ (solid line), $\epsilon_{wav} = 0.02$ (dashed line), $\epsilon_{wav} = 0.015$ (dotted line), $\epsilon_{wav} = 0.01$ (dash-double dotted line). To the right of vertical dash-dotted vertical line transverse rolls bifurcate at onset for $P = 1$

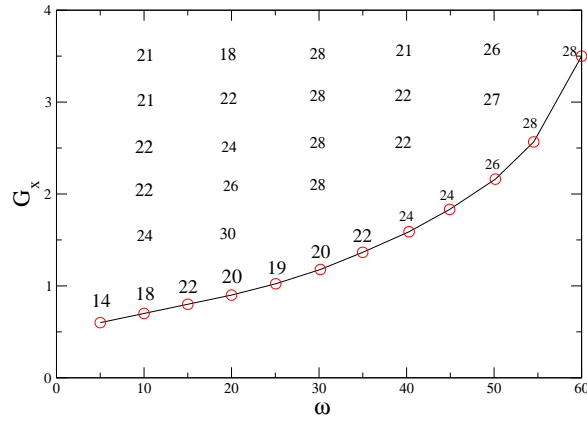


FIGURE 12. Onset of the short wavelength Küppers -Lortz like instability of convection rolls in the circular case as a function of $G_x = G_y$ and of ω . Positive growth rates are found in the limit $\epsilon \rightarrow 0$ above the solid line. The angle $\tilde{\psi}$ of the most unstable mode is indicated.

also been indicated. If one moves vertically up in the diagram at fixed ω the maximal destabilization angle $\tilde{\psi}$ moves through a maximum.

Note that we have not investigated the subtle limiting behavior of the short wave instability line at small ω . This problem would require an analytical WKB-type approach,

which cannot be captured within our numerical method by a finite number of Galerkin modes in the time domain.

The present short wave instability is accessible via a weakly nonlinear analysis as well. We start with the ansatz:

$$\delta\mathbf{V}(\mathbf{x}, z, t) = \exp[\sigma_n t] B(\mathbf{q}_1, t) \mathbf{V}_{lin}(\mathbf{q}_1, z, t) \exp(i\mathbf{q}_1 \cdot \mathbf{x}) \quad (4.10)$$

with $|\mathbf{q}_1| = q_c$. As before we arrive at the amplitude equation

$$\tau_0(\mathbf{q}_1) \sigma_n B = \tilde{\sigma}(\mathbf{q}_1, R) B - a_{11} B |A_0|^2, \quad (4.11)$$

where $\tilde{\sigma}(\mathbf{q}_1, R)$ depends only on the modulus $|\mathbf{q}_1| = q_c$ because of the isotropy in the case of circular shaking. With the use of $|A_0|^2 = \tilde{\sigma}(\mathbf{q}_1, R)/c$ (see (4.3)) we obtain from (4.11):

$$\tau_0(\mathbf{q}_1) \sigma_n(\mathbf{q}_1, R) = \tilde{\sigma}(q_c, R) \left(1 - \frac{a_{11}}{c}\right). \quad (4.12)$$

The condition $a_{11}/c = 1$, where the cross coefficient a_{11} depends on all system parameters and on $\tilde{\psi}$, reproduces to better than 1% the stability line in figure 12, above which $\sigma_n(\mathbf{q}_1, R) > 0$ for $\epsilon \rightarrow 0$.

Finally we like to mention that the present short-wavelength instability in the case of circular shaking tends to rotate the original rolls by a *positive* angle $\tilde{\psi}$ indicated in figure 12, while for a ideal isotropic system $\pm\tilde{\psi}$ would be equivalent. That asymmetry is to be expected since the chiral symmetry is broken by the rotating acceleration. The close analogy to the Küppers-Lortz (KL) instability (Küppers and Lortz (1969); Clever and Busse (1979)) in rotating RBC is obvious. In the latter case the chiral symmetry is broken by the Coriolis force.

5. Numerical simulations in the nonlinear regime

In the previous section we have analyzed the stability of rolls near onset. To study the saturation process of the instability we have employed direct fully 3-dimensional numerical simulations of the basic Eqs. (2.7 -2.11). Our well tested code for standard Rayleigh-Bénard convection (Pesch (1996); Bodenschatz et al. (2000)) has required only minor modifications. The additional time-dependent linear acceleration terms are integrated explicitly in time together with the quadratic nonlinearities. This approach has already been used successfully for vertically shaken convection (Rogers et al. (2005)).

Since the direct simulations consume large amounts of computer resources we have focused the attention on the parameter combination $P = 1$, $G_x = 3.6$ and $\omega = 50$, which would also be convenient for experimental studies as suggested by its use in the vertical shaking case (Rogers et al. (2005)). According to Fig. 3 the longitudinal rolls bifurcate at $R_y = 1708$ with $\mathbf{q}_c = (0, p_c)$ and $p_c = 3.116$ while the onset of transverse rolls is at $R_x = 1773$ for $\mathbf{q}_c = (2.27, 0)$.

First numerical simulations in the unidirectional case for $R = 1.015 R_x \approx 1800$ have

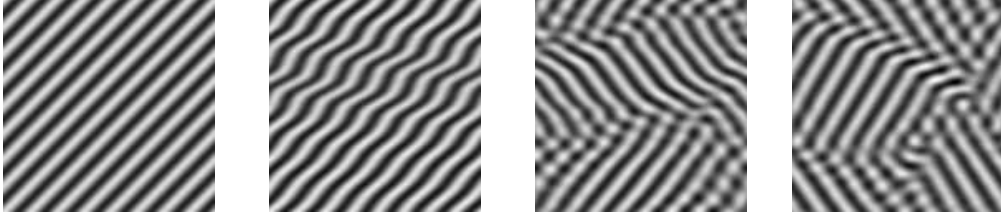


FIGURE 13. Representative snapshots of the temperature modulation Θ in the x, y -plane at $z = 0$ for unidirectional shaking at $\omega = 50, G_x = 3.6, G_y = 0, R = 1.05R_c = 1862, q_c = 2.32$. The time lapse between the pictures (from left to right) is $2t_v$.

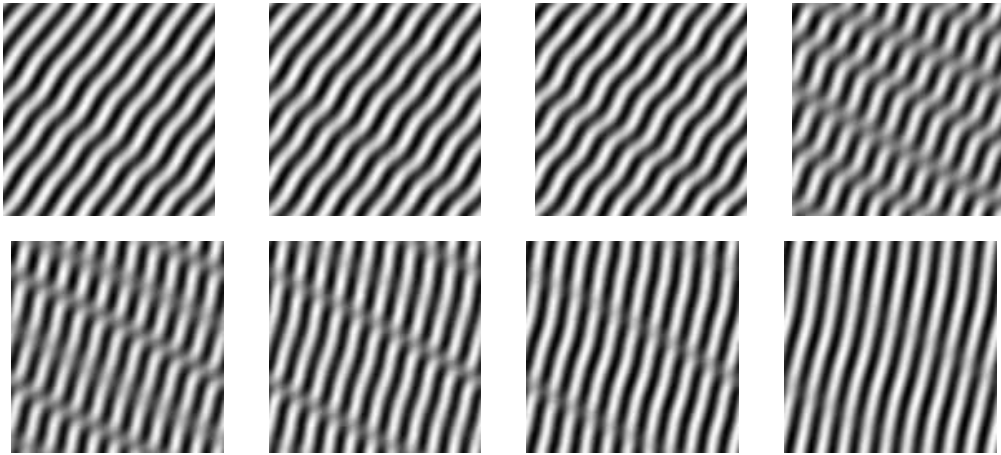


FIGURE 14. Representative snapshots of the heteroclinic orbit in the case of uniformly rotating acceleration for $\Omega = 50, G_x = G_y = 3.6, R = 1.05R_c = 1862, q_c = 2.32$. The timelapse between the pictures (from left to right) is: 2, 2, 4, 6, 4, 2, $2t_v$.

been carried out, where according to figure 11 longitudinal rolls should be unstable against the wavy instability. Indeed, starting the simulations from random initial conditions we did not find longitudinal rolls. Instead the system locked into an oblique roll pattern with wavevector \mathbf{q} with $|\mathbf{q}| = 2.6$ which includes the angle $\chi = \pi/4$ with the x axis (see Fig. 13, 1. panel). We have confirmed the stability of this pattern for $R \leq 1800$ by the Galerkin analysis. At $R = 1810$, however, the pattern becomes unstable against long wavelength modulations with a wavevector \mathbf{s} which includes with \mathbf{q} an angle ψ slightly less $\pi/4$. To study the impact of this instability we have performed a numerical simulation at $R = 1.05 R_c = 1862$. When the simulation is started with the oblique roll pattern obtained at $R = 1800$ and superimposed noise, first the modulational instability becomes visible (see Fig. 13, 2. panel). Continuing the simulation we arrive at a steady dynamic state which is characterized by the coexistence of patches with \mathbf{q} vectors that are oriented mirror symmetrically with respect to the y -direction. As demonstrated in the third and fourth panel of Fig. 13 the patches change chaotically their shape and location. The beaded structure of some rolls points already to the excitation of the mode with the

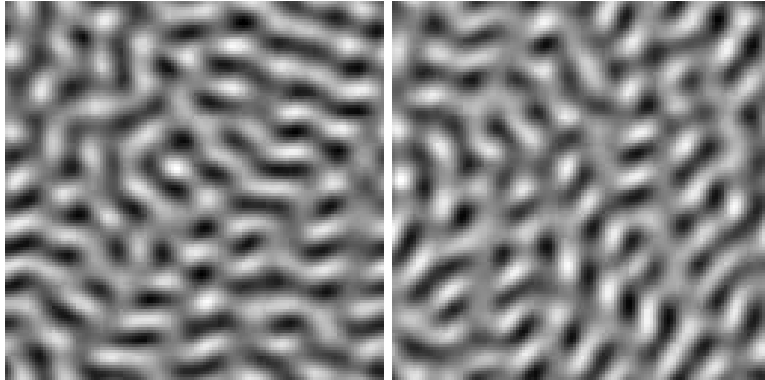


FIGURE 15. Snapshots of disordered patterns (time lapse $4t_v$) for $\omega = 50, G_x = 3.6, Pr = 1, \epsilon = 0.4$ after the destabilization of the heteroclinic orbit in Fig. 14.

respective mirror symmetric \mathbf{q} . This scenario can be understood as follows: The wavy instability of the longitudinal mode with wavevector $\mathbf{q} = (0, p)$ leads to the symmetry degenerate oblique rolls with wavevectors $\mathbf{q} = (\pm q, p)$. By coincidence the simulations have locked into one of these oblique rolls states in Fig. 13, first panel. When these oblique rolls become unstable at $R = 1860$ the system restores the symmetry in the average by producing coexisting patterns with either mode.

In a second set of simulations we have considered the case of circular shaking for the same parameter combinations with $G_x = G_y = 3.6$ at $R = 1862$. According to Fig. 12 the transverse rolls that bifurcate at $R_x = 1773$ are unstable immediately at onset against a KL-type short wavelength instability where one set of rolls is replaced by a new one with the roll axis rotated by a fixed angle $\psi \approx 28^\circ$ for the present parameters. The corresponding simulations are shown in Fig. 14. A persistent rotation of the pattern is seen as is commonly observed for the KL instability. The details are complicated and the cycle passes through patterns with locally distorted rolls and their reconnections. It is illuminating that the angle between the roll axes of the first and the last panel in the series, where the patterns are practically uniform, is about 28° in line with Fig. 12. When ϵ is increased the dynamics becomes increasingly disordered and chaotic (see Fig. 15).

6. Concluding remarks

In this work we have presented a comprehensive analysis of a Rayleigh-Bénard convection setup subjected to a periodic acceleration in the plane. Besides considerably extending an earlier linear analysis of Gershuni et al. (1996) we have investigated the nonlinear regime for the first time. In particular we have identified some specific secondary bifurcations that lead to complex spatio-temporal patterns. The work was partially motivated by recent investigations of a Rayleigh-Bénard system in the presence of vertical oscillations, which is characterized by a variety of quasi-crystalline patterns in excellent

agreement with experiments (Rogers et al. (2005)). It was thus tempting to break the isotropy by uni-directional shaking in the plane and to consider the quasi-isotropic case in the presence of a uniformly rotating acceleration. Because of the broken chiral symmetry in the latter case it has been possible to obtain domain-chaos by a Küppers-Lortz type process in the absence of a Coriolis force.

Because of the numerous parameters of the problem we had to be selective in choosing the examples for the numerical analysis. A guiding principle has been the possible realization in laboratory experiments. Since it is important that in spite of a desirable large aspect ratio the mass of the accelerated part of the apparatus remains small a low height of the fluid layer is essential. This requirement is realized in convection experiments with thin layers of compressed gases such as CO_2 at pressures of the order of 40 bars, which offer also the advantage that the shadowgraph method can be used for visualization. For instance in the experiments of Rogers et al. (2005) on vertical acceleration of a convection layer, a cell height $d = 0.065\text{cm}$ at a mean temperature $T_0 = 308\text{K}$ was used, which corresponds to a vertical diffusion time $t_v \approx 1.65\text{sec}$. Shaking the convection cell with amplitude $b_x \approx 1\text{cm}$ and frequency $f = 4.75\text{Hz}$ corresponds in this case to the dimensionless quantities $\omega = 50$ and $G_x = 3.6$, respectively. It should be emphasized that smaller Prandtl numbers can be reached in gas mixtures (see e.g. Bajaj et al. (2002)) and larger ones in experiments with a gas near its critical point (Assenheimer and Steinberg (1997)).

While layers of pressurized gases offer obvious advantages, horizontal accelerations of thicker layers of convecting liquids to explore larger P might also be attractive, in particular since they can be performed at an ambient pressure. An experiment of this kind has been performed by Kozlow et al. (2004). Unfortunately, only an extended abstract is available which does not provide sufficient information for a comparison with theory. It is hoped that some more systematic experiments can be realized in near future in order to motivate further theoretical exploration of the rich phenomena exhibited by convection in the presence of periodic acceleration.

The research reported in this paper has been supported by the Deutsche Forschungsgemeinschaft (Pe 446/7-1). The help of Dr. P. Akimov in the early stages of the research is gratefully acknowledged.

REFERENCES

- AUER, M. & BUSSE, F. H. 1994 Wavy rolls and their instabilities in extended fluid layers. In *Nonlinear Coherent Structures in Physics and Biology* (ed. Spatschek, K. H. & Mertens F. G) NATO ASI Series: Physics, vol. 329, pp.417-422.
- AUER, M. & BUSSE, F. H. 1997 Wavy rolls in the Taylor-Bénard problem. *Phys. Fluids*, **10**, 318-320.

- ASSENHEIMER, K. E. & STEINBERG, V. 1997 Rayleigh-Bénard convection near the critical point. *Phys. Rev. Lett.*, **70**, 25.
- BAJAJ, K. M., AHLERS, G. & PESCH, W. 2002 Rayleigh-Bénard convection with rotation at small Prandtl numbers. *Phys. Rev. E*, **65**, 056309.
- BODENSCHATZ, E., PESCH, W. & AHLERS, G. 2000 Recent developments in Rayleigh-Bénard convection. *Ann. Rev. Fluid Mech.*, **32**, 709–778.
- CHANDRASEKHAR, S. 1961 *Hydrodynamic and Hydromagnetic Stability*, Clarendon Press, Oxford
- CLEVER, R. M. & BUSSE F. H. 1979 Nonlinear properties of convection rolls in a horizontal layer rotating about a vertical axis *J. Fluid. Mech.*, **94**, 609–627.
- CLEVER, R. M. & BUSSE, F. H. 1977 Instabilities of longitudinal convection rolls in an inclined layer. *J. Fluid Mech.*, **81**, 107–125.
- DANIELS, K. E. AND BODENSCHATZ, E. 2002 Defect turbulence in inclined layer convection. *Phys. Rev. Lett.*, **88**, 034501.
- CROSS, M. C. AND HOHENBERG, P. C. 1993 Pattern formation outside of equilibrium. *Rev. Mod. Phys.*, **65**, 875.
- GERSHUNI, G.Z., KELLER, I.O., AND SMORODIN, B.L. 1996 Vibrational and Convective Instability of a plane horizontal fluid layer at finite vibration frequencies. *Fluid Dynamics* **31**, 666–671. (transl. from *Izvest. R. Akad. Nauk., Mekh. Zhid. i Gaza* **5**, 41-51 (1996))
- GERSHUNI, G.Z., AND LYUBIMOV, D.V. 1998 *Thermal Vibrational Convection*, John Wiley and Sons Ltd.
- KOZLOV A.A., BABUSHKIN I. A., AND PUTIN G.F 2004. The Influence of Translational Vibrations of Circular Polarization on Fluid Convective Instability and Flow Patterns *Proceedings of 21st International Congress of Theoretical and Applied Mechanics. Warsaw, Poland. 2004*
- KÜPPERS, G. & LORTZ, D. 1969 Transition from laminar convection to thermal turbulence in a rotating fluid layer. *J. Fluid Mech.*, **35**, 609–620.
- A. C. OR 1997 Finite wavelength instability in a horizontal liquid layer on an oscillating plane. *J. Fluid Mech.*, **335**, 213–335.
- PESCH, W. 1996 Complex spatiotemporal convection patterns *Chaos* **6**, 348–357.
- ROGERS, J.L., BRAUSCH, PESCH, W. & SCHATZ, M.F. 2000 Super lattice patterns in vertically oscillated thermal convection. *Phys. Rev. Lett.* **85**, 4281–4284.
- ROGERS, J.L., PESCH, W. & SCHATZ, M.F. Pattern formation in vertically oscillated convection. *Nonlinearity* **16**, C1- C10.
- ROGERS, J.L., PESCH, W., BRAUSCH, O. & SCHATZ, M.F. 2005 Complex-ordered Patterns in Shaken Convection. *Phys. Rev. E* **71**, 066214-1–18.
- SCHULZE, T.P. 1999 A note on subharmonic instabilities. *Phys. Fluids* **11**, 3573–3576.